Article

A novel-structure LC resonant passive wireless sensor for NO_2 sensing

Zhiyang Liu, Yanbai Shen *, Sikai Zhao *, Jinzhou Bai, Ruixue Ma, Shuling Gao, Wengang Liu, Qiang Zhao

School of Resources and Civil Engineering, Northeastern University, Shenyang 110819, China
* Correspondence: shenyanbai@mail.neu.edu.cn (Y. Shen); zhaosikai@mail.neu.edu.cn (S. Zhao)

Abstract: This work presents an LC resonant passive wireless gas sensor with a novel structure designed to mitigate the negative impact of substrate. The LC sensor antenna with the new structure and the reader antenna were designed and optimized utilizing HFSS software to improve the transfer efficiency. The superiority of the designed structure compared with the general ones is highlighted and verified. The change in the substrate capacitance has essentially no interference with the parameters to be measured of the LC sensor. The sensor with the new structure was prepared by combining etching and sputtering methods. The structure of the ZnO nanowires (NWs) was characterized to confirm their high purity and wurtzite crystal structure. The LC gas sensors demonstrated excellent wireless sensing performance including a low detection limit of 0.5 ppm NO_2, high response of 1.058 and outstanding stability at 180 °C. The developed new sensor structure not only prevented interference from the substrate during gas sensing testing, but also expanded the choice of sensor substrates, playing a critical role in the development of sensors based on LC resonance principle.

Keywords: LC gas sensor; novel structure; ZnO nanowires; NO_2

1. Introduction

Nitrogen dioxide (NO_2) is a significant atmospheric contaminant primarily generated via the combustion of diverse fuels such as coal, chemicals, and natural gas in power generation facilities [1,2]. Large amounts of NO_2 exhaust have severe detrimental effects on the environment and human health, ranging from acid rain, photochemical smog, global warming to respiratory problems [3-5]. Due to the safety hazards and excessive size of conventional gas detection devices, it is very difficult to detect NO_2 in some special application scenarios, such as flammable and explosive, rotating, and confined spaces. As such, there is a great demand for a wireless and passive gas sensor to enable effective monitoring. To date, various wireless sensing devices have been created to monitor harmful gases, which use different measuring mechanism such as surface acoustic wave (SAW) [6-8], wireless passive LC resonance [9,10], and microwave evanescent mode [11,12] , etc.

The wireless passive inductor-capacitor (LC) resonant approach is more optimal for these special application scenarios because it facilitates energy conversion and data reading due to its lower operating frequency and stable signal transmission capability [13]. Gas sensors based on the LC resonance principle are increasingly popular due to their ease of readout for measured concentration and low installation costs [14]. Such sensors consist of LC antennas and gas sensing materials. When the gas parameter to be measured alters, the electrical properties of the gas sensing material will be changed, which in turn causes a variation in the input impedance of the sensor. Non-contact testing of the sensor signal can be achieved via an external signal reading system connecting a reader antenna to the sensor in a near-field coupling [15].

 doi:10.20944/preprints202305.0866.v1

The use of LC sensors for gas detection has been extensively researched in numerous studies. For instance, Azzarelli et al. combined gas sensing materials with near field communication (NFC) tags and converted the gas sensing analog signal into a digital signal to recognize NH_3 in confined environments via smartphones [16]. Ma et al. utilized low-temperature cofired ceramic (LTCC) technology to fabricate LC gas sensors for NO_2 gas sensing [17]. Ma et al. developed a high-performance nanostructured conductive polymer as a switch material of NFC tags to enable the detection of NH_3 [18]. Overall, current research efforts primarily concentrate on the innovation of application [19,20], the preparation process of sensor and substrate materials [21], and synthesis of gas sensing materials [22,23]. The structure of LC gas sensors is relatively homogeneous, namely gas sensing materials being coated on the interdigital capacitors (IDC) directly or coated after adding a dielectric layer. It is inherently deficient due to the direct contact between the underside of the IDC and the substrate. Changes in the physical properties of the substrate can significantly affect the measured parameters. Our previous work had explored the use of high-performance ZnO nanowires (NWs) with wurtzite structure [24,25]. However, it is still a major challenge to optimize the sensor structure so that the existing high-performance gas sensing materials can be effectively combined with the LC resonant circuit to achieve low-cost, accurate, efficient, and stable wireless NO_2 gas monitoring [26].

In this work, a novel LC sensor structure was developed in which the IDC of the sensor no longer contacted the substrate. The advantages of this structure were discussed and verified, and the sensor structure was implemented using a combination of etching and sputtering methods. The LC antenna and reader antenna were designed and optimized by utilizing HFSS, and good signal transmission was obtained. This work provides a new sensor structure based on the principle of mutual inductive.

2. Experimental

2.1. Design and Optimization of Antennas

The frequency design of sensor antennas not only requires a consideration of the application scenario, but also demands an evaluation of the material of the substrate. In this work, FR4 was used as the substrate, which had a very low dielectric constant of 4.4 and showed a very fast signal transmission rate. Nonetheless, an excessively high operating frequency may lead to the substantial losses. Thus, a careful consideration should be given to ensure that the operating frequency remains below 0.5 GHz [27].

The relationship between the operating frequency (f_o) of an LC antenna and its inductance (L_S) and capacitance (C_S) values can be expressed as follows [17].

$$f_o = \frac{1}{2\pi\sqrt{L_S C_S}} \tag{1}$$

Here, the values of L_S and C_S are reliant upon the structural dimensions of the circuit [17].

$$L_S = 1.39 \times 10^{-6}(d_0 + d_i)N_i^{5/3}\, log\left(4\frac{d_o + d_i}{d_o - d_i}\right) \tag{2}$$

$$C_S = l_c(N_c - 1)\varepsilon_0 \frac{1 + \varepsilon_r K\left[(1 - (d_s/d_c)^2)^{1/2}\right]}{2K(d_s/d_c)} \tag{3}$$

Where N_i is the number of loops, d_o and d_i denote external and internal coil widths of the inductor, respectively. l_c represents the length of the IDC fingers, N_c refers to the count of contact points on IDC each terminal. ε_0 denotes the air permittivity. ε_r is the dielectric constant of the FR4 substrate. d_s refers to the width of the orifice be-

Preprints (www.preprints.org) | NOT PEER-REVIEWED | Posted: 11 May 2023 doi:10.20944/preprints202305.0866.v1

tween two neighboring fingers, while d_c represents the total spacing between two adjacent fingers. K is a mathematical function known as the complete elliptic integral of the first kind.

A three-dimensional model was established and simulated via HFSS. To fulfill the operating frequency specifications, it may be necessary to tune the size of the LC antenna. A flat helical inductor and IDC are connected through vias on the substrate to form a resonant circuit with ZnO NWs employed as the gas sensing material (Figure 1). Upon exposure to NO_2 molecules, the charge transfer takes place and then alters the S_{11} of the LC resonant circuit. The designed parameters of LC antenna are displayed (Table 1).

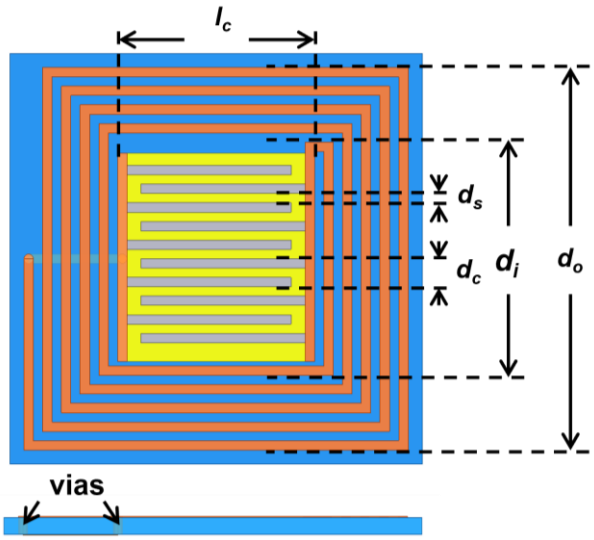

Figure 1. Schematic diagram of the LC gas sensor.

Table 1. Parameters of the designed LC antenna.

l_c	d_c	d_s	N_i	d_o	d_i	N_c
10.5 mm	1.5 mm	0.5 mm	4.75	20.5 mm	12.5 mm	5

HFSS software can be utilized to determine both the size and height of the reader antenna. The smaller the S_{11} parameter, the higher the signal or energy transfer between the reader antenna and the LC antenna. The simulation outcome of the S_{11} parameter under various side lengths of the reader antenna (Figure 2a) demonstrates that when the reader antenna is set to $(d_o + d_i)/2$, S_{11} has the smallest value of -11.1 dB. The simulation results for different read heights with a side length of $(d_o + d_i)/2$ is showed (Figure 2b). At a reading height of 5 mm, the value of S_{11} is a minimum of -19.2 dB. This value indicates a slight signal and energy loss between the LC antenna and the reader antenna.

The resistance variation of ZnO NWs was simulated to replicate the actual exposure to NO_2, whereas alterations in the S_{11} of the LC sensor were monitored. It is discernible that the S_{11} parameter of the designed LC antenna diminishes in a certain pattern with the rise of leakage resistance of the sensor (Figure 2c), demonstrating the design agreement with the requirements. Therefore, the LC antenna and the reader antenna were prepared according to the structural parameters.

A reading height of 5 mm was selected to test the LC antenna. The operating frequency of the antenna is 156.8 MHz, which satisfies the frequency requirements below 0.5 GHz. Deviations between the simulated and measured values are mainly attributed to parasitic effects [28]. At the operating frequency, the VSWR of the LC antenna is observed to be 1.238 (Figure 2d), which is less than 1.5, thus confirming that the designed antenna can effectively transfer energy and information with the reader antenna.

Preprints (www.preprints.org) | NOT PEER-REVIEWED | Posted: 11 May 2023 doi:10.20944/preprints202305.0866.v1

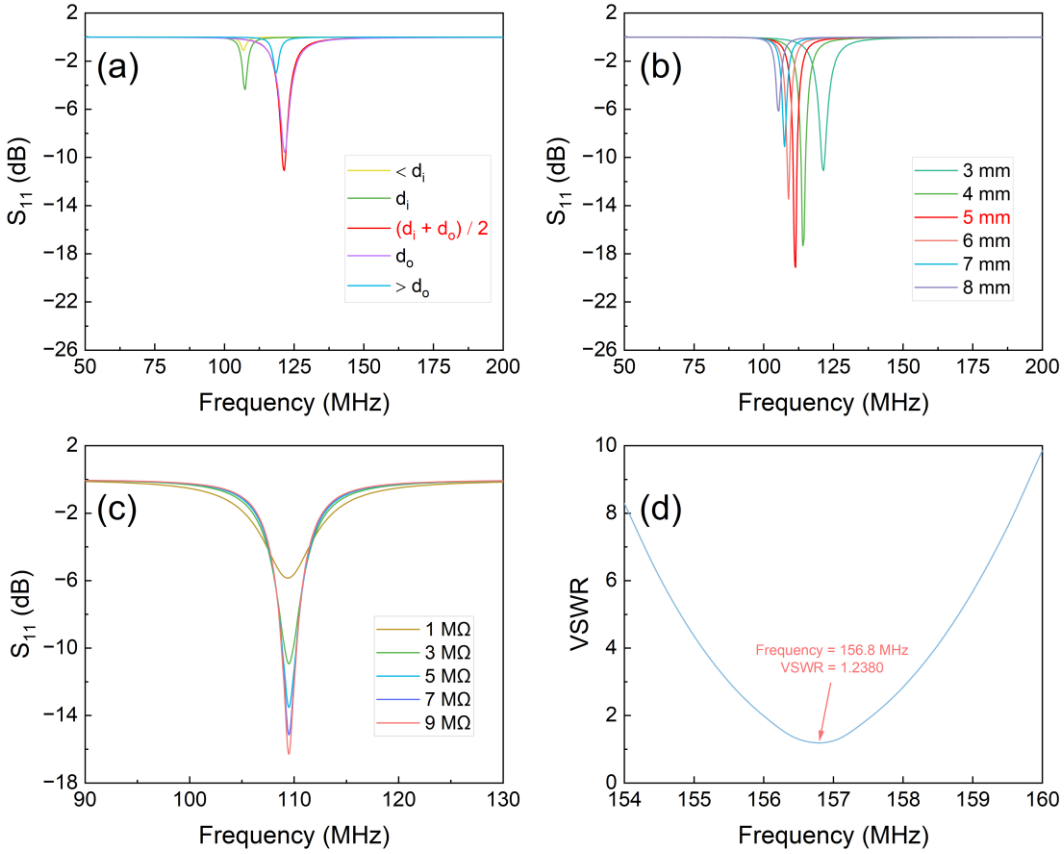

Figure 2. (a) Side length optimization of the reader antenna; (b) Height optimization of the reader antenna; (c) Variation of S_{11} of the LC antenna; (d) VSWR result of the LC antenna.

2.2. Synthesis and Characterization of ZnO NWs

ZnO NWs were produced using a solvothermal method. Specifically, combine 2.5 g of NaOH, 0.1 g of SDS, and 0.44 g of Zn $(CH_3CO_2)_2{\cdot}2H_2O$ in 117 ml of ethanol and mix well until the components are fully dissolved. Then, add 27 ml of PEG400 to the mixture and stir thoroughly. The resulting solution was heated to 140 °C for 16 h. Following this step, the white sediment was gathered by centrifugation and washed several times to completely rid it of residual organic and inorganic ions, and eventually dried at 60 °C. The dried samples were then annealed in a tubular furnace for 3 h at a temperature of 500 °C. Subsequently, natural cooling of the samples to room temperature was carried out to achieve ZnO NWs for LC gas sensors.

The crystalline phases, microscopic morphology, and surface chemistry of the ZnO NWs were characterized by using an X-ray diffractometer (XRD-7000), scanning electron microscope (TESCAN MIRA LMS), transmission electron microscope (FEI Tecnai G2 F20) and X-ray photoelectron spectrometer (Thermo Scientific K-Alpha X). Additionally, the selected area electron diffraction (SAED) patterns were recorded for further analysis.

2.3. LC Sensor Fabrication and Gas Sensing Measurement

The Schematic diagram of the manufacturing process of the LC gas sensor is showed (Figure 3).The inductor was processed on an FR4 substrate with the etching method to obtain the LC antenna after ultrasonic cleaning for 10 min. Subsequently, the ZnO NWs were uniformly coated on the FR4 substrate, and the substrate with the gas sensing material was placed in an oven for drying. After natural cooling, a plasma sputtering device was used to sputter platinum electrodes on its surface. Finally, the LC sensor was aged at 200 °C for 6 h.

Preprints (www.preprints.org) | NOT PEER-REVIEWED | Posted: 11 May 2023 doi:10.20944/preprints202305.0866.v1

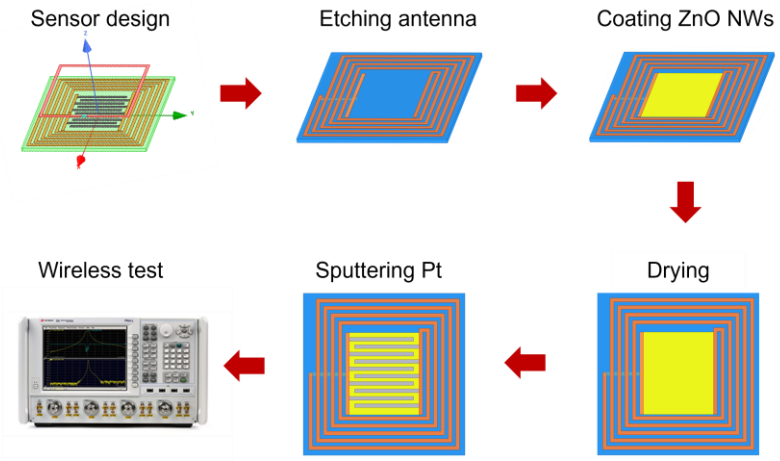

Figure 3. Schematic diagram of the manufacturing process of the LC gas sensor.

Schematic diagram of the wireless gas sensing measurement setup is showed (Figure 4a). The LC gas sensor was positioned on a temperature-controlled heating table within a sealed gas chamber, while an external reader antenna was connected to a VNA (AV3656D) and placed parallel to the sensor at around 5 mm. This configuration enabled precise measurement and analysis of the sensor's response to the presence of NO_2 gas. Subsequently, the network analyzer is used to analyze the information collected by the reader antenna. Measurements of the S_{11} and corresponding frequency (f_o) were recorded at regular 10-second intervals. The response of the LC sensor was determined as S_{11g}/S_{11a}, in which S_{11a} and S_{11g} represent the S_{11} of the LC sensor in air and in NO_2, respectively (Figure 4b). The determination of the response and recovery times of the sensor involves measuring the duration needed for a 90 % alteration in the fully normalized S_{11} amplitude. To compare responses, all measured S_{11} were divided by the initial S_{11} magnitude, resulting in a "normalized S_{11}" that started from -1.0. This approach ensured that all baselines originated at the same value, irrespective of any added mass attributable to the sensitive layer [29].

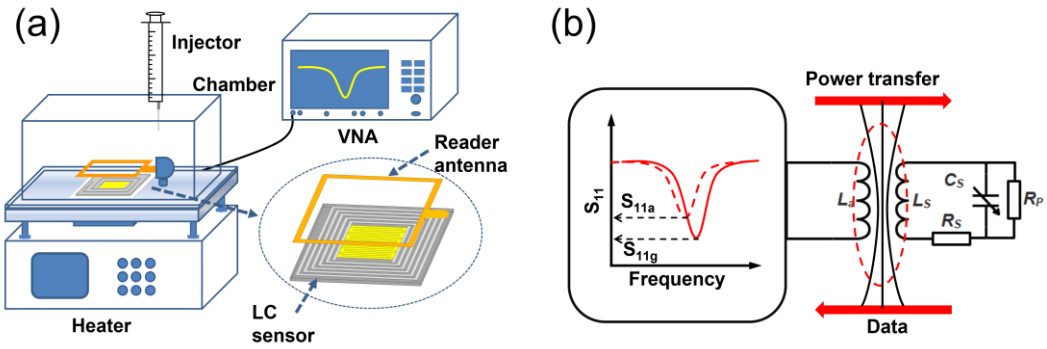

Figure 4. (a) Schematic diagram of the wireless gas sensing measurement setup; (b) Equivalent circuit of the wireless gas sensing measurement.

In the equivalent circuit of the radio signal transmission (Figure 4b), R_a and R_s represent the series resistances of the reader antenna and the sensor, respectively. R_p is the leakage resistance of the IDC, which is equivalent to the parallel resistance of the C_s. L_a is the inductance of the reader antenna, while L_s is the inductance of the sensor. k represents degree of coupling between the reader antenna and the sensor, which is related to the relative position of the two inductors, was assumed to be constant during the measurement process, and therefore could be considered as a fixed value. The relationship between the input impedance (Z_a) and the above parameters can be expressed by equations

Preprints (www.preprints.org) | NOT PEER-REVIEWED | Posted: 11 May 2023 doi:10.20944/preprints202305.0866.v1

(4)-(6) [30], indicating that changes in both C_s and R_p affect the change in Z_a in the circuit. The change of Z_a in this work depends mainly on the change of R_p, which are brought about by the interaction between NO_2 molecules and ZnO NWs. It can be inferred from equation (7) that S_{11} is equivalent to Z_a. As such, monitoring changes in the S_{11} parameter may provide valuable insights into variations in gas properties.

$$Z_a = Z' + jZ'' = \frac{\omega^2 k^2 L_s L_a A}{A^2 + B^2} + j\left(\omega L_a - \frac{\omega^2 k^2 L_s L_a B}{A^2 + B^2}\right) \tag{4}$$

$$A = R_s + \frac{R_p}{1 + \omega^2 C_s^2 R_p^2} \tag{5}$$

$$B = \omega L_s + \frac{\omega C_s R_p^2}{1 + \omega^2 C_s^2 R_p^2} \tag{6}$$

$$S_{11} = (Z_a - Z_0)/(Z_a + Z_0) \mid Z_0 = 50\ \Omega \tag{7}$$

3. Results and Discussion

3.1. Novel Structure of the LC Sensor

The structure of the LC sensor (Figure 5a) and physical diagram of the LC sensor (Figure 5b) are showed respectively. Generally, the IDC is processed firstly, followed by the application of the gas sensing material. In contrast, this approach involves coating the gas sensing material onto the substrate and then sputtering the platinum on the IDC once the material has been fully adhered to the substrate. The most significant departure of this special structure from its conventional counterpart lies in the fact that the IDC no longer directly contact the substrate.

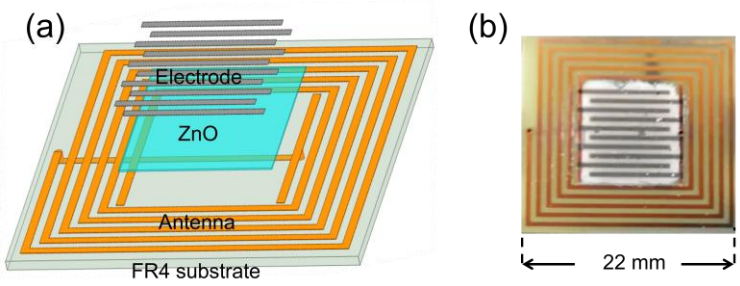

Figure 5. (a) Structure diagram of the LC sensor; (b) Physical picture of the LC sensor.

Comparing the two sensor structures, the equivalent circuit diagrams are shown (Figure 6). In the general structure (Figure 6a), R_1 and R_2 represent the leakage resistances of the IDC, while R_p denotes the parallel resistance of R_1 and R_2. Additionally, C_S refers to the total capacitance of C_1 and C_2 arranged in parallel. In comparison, in this work (Figure 6b), R_1 and R_3 are the leakage resistances of the IDC, while R_p represents the parallel resistance of R_1 and R_3. Furthermore, C_S corresponds to the total capacitance of C_1 and C_3 arranged in parallel. Herein, R_1 and C_1, R_2 and C_2, and R_3 and C_3 represent the equivalent resistance and capacitance of gas sensing material, substrate, and free space, respectively. In practical application, R_1 and C_1 of the gas sensing material will alter with changes in gas concentration. As for R_2 and C_2, they will change due to the differences in the substrate, and C_2 will also change because of variations in gas adsorption by the substrate. However, R_3 and C_3 remain relatively constant. Equations (4)-(7) reveal that, for the general coating method (Figure 6a), changes in the substrate and C_2 during the testing process will interfere with the alteration of C_S, thereby potentially affecting test results. In contrast, the structure utilized in this work (Figure 6b)

Preprints (www.preprints.org) | NOT PEER-REVIEWED | Posted: 11 May 2023 doi:10.20944/preprints202305.0866.v1

involves the upper surface of the IDC contacting the surrounding air. As a result, C_3 and R_3 remain nearly unchanged, thus eliminating interference from the substrate.

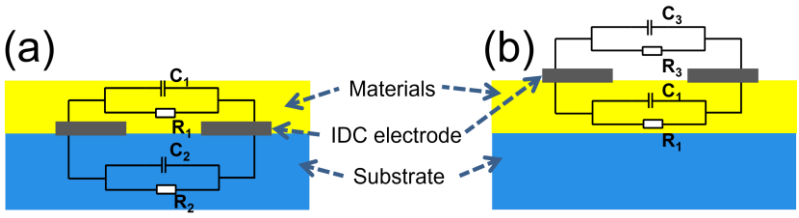

Figure 6. Comparison of two gas sensor structures. (a) Contacted; (b) Uncontacted.

Verification was conducted via HFSS software simulation. A fixed resistance 'box' was employed to simulate the gas sensing material. It was separately placed above and below the IDC to build the two different structures. Additionally, a variable capacitance 'sheet' was positioned above the substrate to replicate alterations in C_2, with a change range set between 3.5-4.5 pF. Simulation was executed to observe both the S_{11} parameter of the sensor antenna and the change in resonant frequency f_0 using the $f - S_{11}$ curve.

The variation of S_{11} and f_0 of the sensor with two different structures is showed (Figure 7). For clarity, S_{11} and f_0 values extracted at a capacitance of 3.5 are selected as initial values (S_I and f_I). Equations 8-9 express the changes in S_{11} and f_0, denoted as S_V and f_V, respectively. It is noteworthy that the S_{11} (Figure 7a) and f_0 (Figure 7b) values of the LC sensor, utilizing the proposed sensor structure, exhibit minimal sensitivity to changes in substrate capacitance of C_2.

$$S_V = \frac{S_{11} - S_I}{S_I} \tag{8}$$

$$f_V = \frac{f_0 - f_I}{f_I} \tag{9}$$

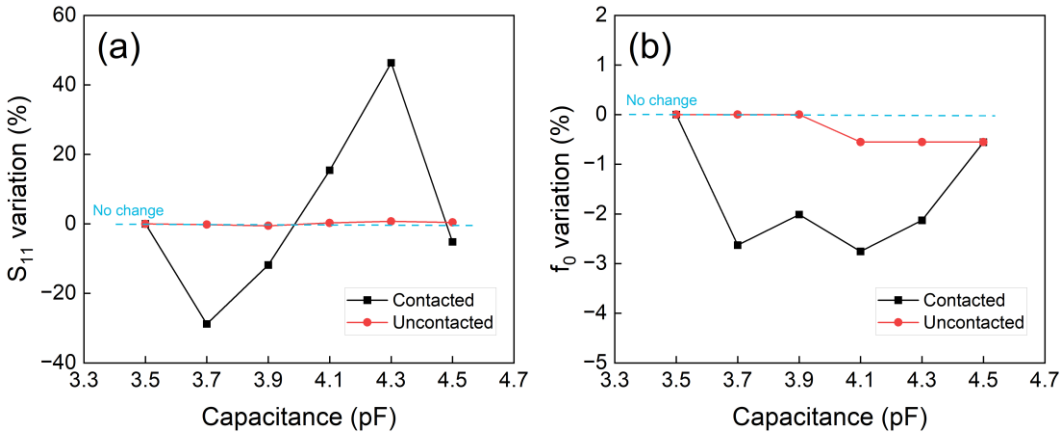

Figure 7. Effect of capacitance variation on (a) S_{11} and (b) f_0 for two different structures.

The simulation results provide clear evidence that the proposed sensor structure outperforms the conventional one, thereby effectively mitigating the detrimental effects of substrate gas adsorption on gas sensing testing. Furthermore, such new structure can extend the range of substrate options for LC sensor.

3.2. Characterizations of ZnO NWs

The XRD pattern of the as-synthesized sample (Figure 8) indicated that the obtained samples are high purity ZnO with hexagonal wurtzite structure (ICDD #99-0111) [31]. The as-prepared sample was observed by SEM and TEM (Figure 9). The ZnO samples exhibit

Preprints (www.preprints.org) | NOT PEER-REVIEWED | Posted: 11 May 2023 doi:10.20944/preprints202305.0866.v1

a uniform and wire shape with smooth and non-branched surfaces and excellent dispersion (Figure 9a-c). The ZnO products display a narrow diameter distribution, ranging from 20-50 nm. Additionally, for a single ZnO NWs, the diameter displays hardly any variation along the long axis. The length distribution of the ZnO NWs is slightly wider, ranging from 500 nm to a few micrometers. The excellent crystallinity of the synthesized ZnO NWs is evident from the clear diffraction fringe observed (Figure 9e), where the interplanar spacing between adjacent fringe is 2.6 Å. Based on the XRD results, it is determined that this spacing corresponds to the (002) crystal plane of the hexagonal fibrillated ZnO structure. This results indicates that the ZnO NWs are formed by the growth of ZnO grains along the c-axis direction (Figure 9d) [32]. Furthermore, the SAED pattern of the ZnO NWs (Figure 9f) displays a distinct diffraction dot pattern, providing evidence for the single-crystal nature of the as-prepared ZnO NWs.

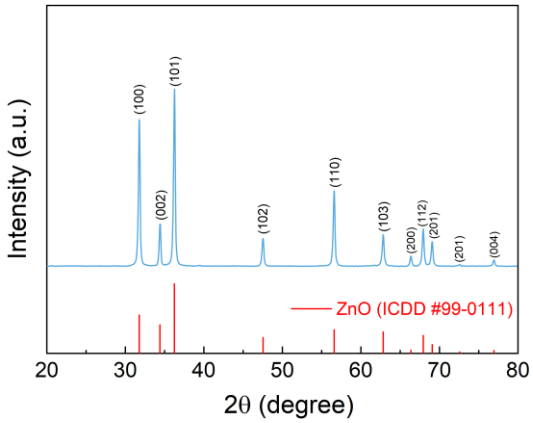

Figure 8. XRD pattern of ZnO NWs.

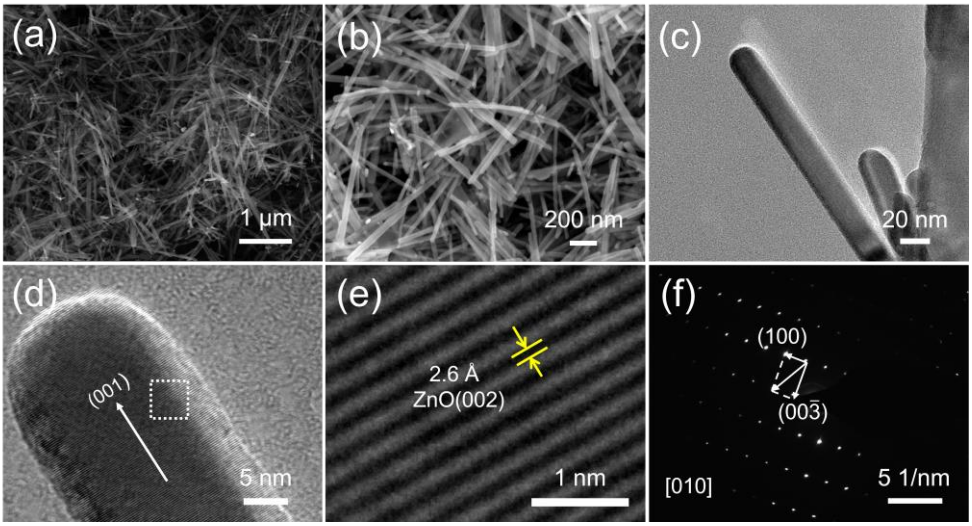

Figure 9. (a, b) SEM images, (c-e) TEM images, and (f) SAED pattern of ZnO NWs.

The XPS analysis results of the ZnO NWs is showed (Figure 10). The full spectrum scan (Figure 10a), indicating the presence of spectral peaks for Zn, O, and C elements only, further confirming high purity of the ZnO NWs. The high-resolution spectrum of Zn 2p (Figure 10b) reveals two distinct characteristic peaks. The peak at a binding energy of approximately 1021.27 eV corresponds to Zn $2p_{3/2}$, while the peak at a binding energy of about 1044.33 eV corresponds to Zn $2p_{1/2}$, with an energy interval of approximately 23 eV between them. This indicates that the element Zn in the ZnO NWs exists in the +2 valence form [33]. In the high-resolution spectrum of O 1s (Figure 10c), the observed peak at a binding energy of approximately 530.02 eV is caused by lattice oxygen in ZnO crystals.

Preprints (www.preprints.org) | NOT PEER-REVIEWED | Posted: 11 May 2023 doi:10.20944/preprints202305.0866.v1

Additionally, the peaks at binding energies of around 531.04 eV and 536.04 eV are primarily associated with adsorbed oxygen on the material surface as well as oxygen vacancies [34,35].

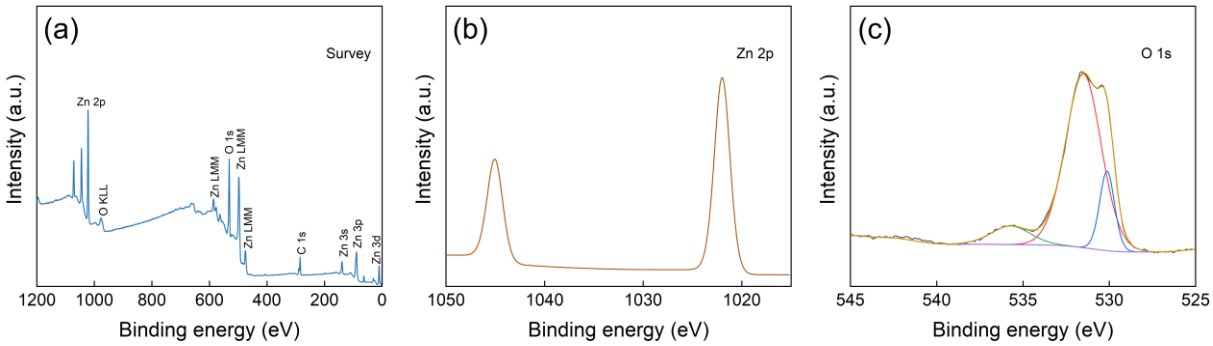

Figure 10. XPS spectra of ZnO NWs. (a) Survey scan spectrum; (b) Zn 2p spectrum; (c) O 1s spectrum.

3.3. NO_2 Sensing Properties of the LC Sensor

According to the electrical model presented in previous reports, by analyzing the S_{11} and f_o data acquired from the reader antenna, it is possible to infer changes in the surrounding environment. The $f - S_{11}$ curves of the substrate alone, the LC antenna, and the LC gas sensor in both air and NO_2 environments at an operating temperature of 180 °C is measured (Figure 11). A pronounced decline in f_o and S_{11} amplitude can be observed when comparing the LC gas sensor to the LC antenna, both in air. This is attributable to the fact that ZnO possesses higher dielectric constant and conductivity values compared to those of air. The coating of ZnO on the IDC leads to an increase in its capacitance and a decrease in its leakage resistance. In comparison to the sensor in air, the f_o and S_{11} magnitudes of the sensor increase following exposure to NO_2. This increase is primarily attributed to the adsorption of NO_2 on the ZnO NWs, which subsequently changes the input impedance of the circuit and thereby modifies the f_o and S_{11}. Moreover, it is evident that the S_{11} of the LC sensor exhibit a measurement value of less than -10 dB both before and after exposure to NO_2. This observation further confirms the high energy and information transfer efficiency of LC gas sensor with the reader antenna.

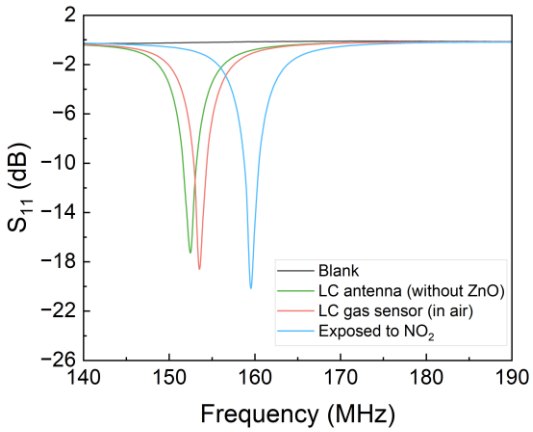

Figure 11. Frequency response of the LC antenna, LC gas sensor, and the reference templates in air and in NO_2.

The operating temperature has the greatest effect on the gas sensing properties of the LC gas sensor based on metal oxide semiconductor, therefore the response of the LC sensor at variable temperatures was initially evaluated [36,37]. The response variation of the LC gas sensor to 1 ppm NO_2 across an operating temperature range of 60-210 °C (Figure

Preprints (www.preprints.org) | NOT PEER-REVIEWED | Posted: 11 May 2023 doi:10.20944/preprints202305.0866.v1

12a). As the operating temperature of the sensor increases, its response exhibits a gradual rise and reaches a peak value at 150 °C, after which it decreases gradually with further increases in the operating temperature. This phenomenon can primarily be attributed to the significant effect of operating temperature on both the number of surface-active sites of the ZnO NWs and the kinetics of gas adsorption and reaction [38].

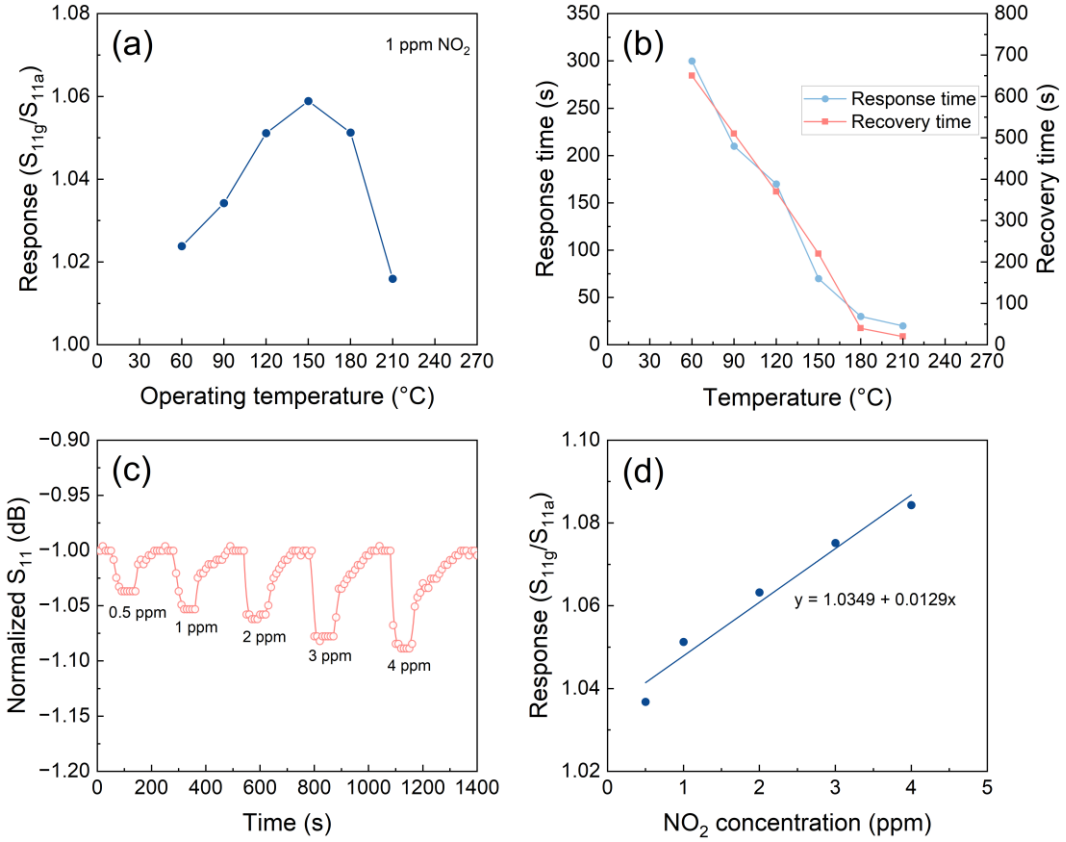

Figure 12. (a) Sensor response and (b) response/recovery times of the LC sensor to 1 ppm NO_2 at different operating temperatures; (c) Response-recovery curves and (d) sensor response of the LC sensor to different concentrations of NO_2 at 180°C.

The response/recovery times of the LC sensor were assessed at different operating temperatures for detecting 1 part per million (ppm) concentration of NO_2 (Figure 12b). The response/ recovery times of the LC gas sensor decrease rapidly with increasing operating temperature. This phenomenon can primarily be attributed to the significant acceleration of NO_2 molecule adsorption and desorption processes on the ZnO NWs at higher operating temperatures, effectively shortening the response/recovery times. However, it should be noted that the sensor response decreases at excessively high temperatures. Therefore, a suitable combination of the LC sensor response and response/recovery times is necessary when determining the suitable operating temperature of the sensor [39]. In this work, the LC gas sensor exhibits its maximum response to 1 ppm NO_2 at 150 °C with a value of 1.058, with only a minor difference in response observed at 180 °C with a value of 1.051. However, notable discrepancies are observed in the response/recovery times at 180 °C compared to that recorded at 150 °C. Therefore, it is determined that the optimal operating temperature of the designed LC sensor is 180 °C.

To thoroughly examine the gas sensing capabilities of the LC sensor at its optimal operating temperature, response and recovery curves were obtained for a range of NO_2 concentrations (0.5, 1, 2, 3, and 4 ppm) (Figure 12c). These measurements provided a comprehensive understanding of the sensor's performance under varying NO_2 concentrations. The LC gas sensor exhibits excellent response-recovery characteristics across a range of

Preprints (www.preprints.org) | NOT PEER-REVIEWED | Posted: 11 May 2023 doi:10.20944/preprints202305.0866.v1

NO_2 concentrations. Additionally, the response of the LC sensor to different concentrations of NO_2 at 180 °C was demonstrated (Figure 12d). Notably, a strong linear relationship between the response and NO_2 concentration is observed within the concentration range of 0.5-4 ppm. This observation suggests that the designed sensor may be well-suited for quantitative detection and analysis of NO_2. It is also noteworthy that the LC gas sensor is capable of effectively detecting NO_2 at extremely low concentrations of 0.5 ppm. This underscores the potential value of the LC gas sensor in various industrial and environmental applications.

Given their passive property, the LC gas sensors are highly suitable for use in scenarios where battery replacement is impractical or difficult. However, this feature also presents a challenge to the stability of such sensors, as their reliability and long-term performance must be maintained without the benefit of regular power source maintenance. The response-recovery curves of the LC sensor to 1 ppm NO_2 at 180 °C over five consecutive tests are shown (Figure 13a). The sensor exhibits consistent response-recovery characteristics across each test cycle. Furthermore, the S_{11} parameter of the sensor can revert to its initial value after each test, indicating an excellent reversibility, repeatability, and stability. To further assess the stability of the sensor over a longer time, the changes in sensor response to 1 ppm NO_2 over a 60-day timeframe were recorded (Figure 13b). Notably, it is observed only minor fluctuations in the response of the sensor over this extended period, underscoring its exceptional stability for detecting NO_2 at 180 °C.

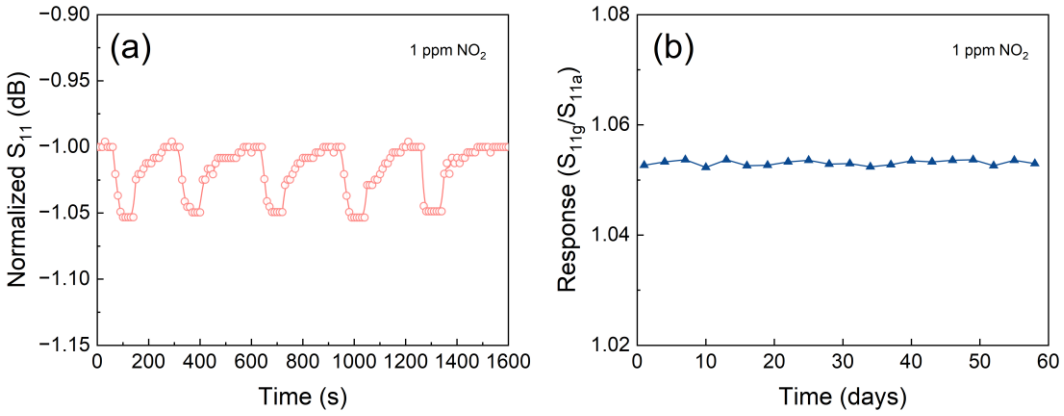

Figure 13. (a) Response-recovery curves of the LC sensor to 1 ppm NO_2 at 180 °C over five consecutive tests; (b) Response of the LC sensor to 1 ppm NO_2 at 180 °C in 60 days.

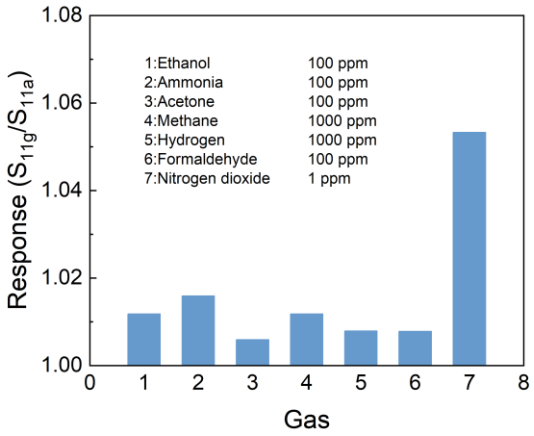

Figure 14. Responses of the LC sensor to different types of gases.

To further investigate the selectivity of LC sensors for different kinds of gases, the responses of the sensor towards different gases are evaluated at the optimal operating temperature. The response of the LC sensor towards NO_2 at 180 °C is significantly higher

Preprints (www.preprints.org) | NOT PEER-REVIEWED | Posted: 11 May 2023 doi:10.20944/preprints202305.0866.v1

than that of other tested gases (Figure 14), indicating exceptional NO_2 selectivity of the developed LC gas sensor.

3.4. Gas Sensing Mechanism of the LC Sensor

The gas sensing mechanism of the LC gas sensor to NO_2 is briefly described (Figure 15). When the sensor is in air, a significant number of oxygen molecules are adsorbed on the surface of ZnO NWs in the form of chemisorbed oxygen of O_2^-, O^-, or O^{2-} [40,41]. These adsorbed oxygen species trap electrons from the conduction band of the ZnO NWs, resulting in the formation of an electron depletion layer on the ZnO surface and a subsequent decrease in carrier concentration. As a result of these changes, the resistance of the material increases, with the corresponding chemical reaction equations shown in equations 10-13 [42,43].

$$O_2(g) \rightarrow O_2(ads) \quad (10)$$

$$O_2(ads) + e^- \rightarrow O_2^-(ads) \quad (11)$$

$$O_2(ads) + 2e^- \rightarrow 2O^-(ads) \quad (12)$$

$$O_2(ads) + 4e^- \rightarrow 2O^{2-}(ads) \quad (13)$$

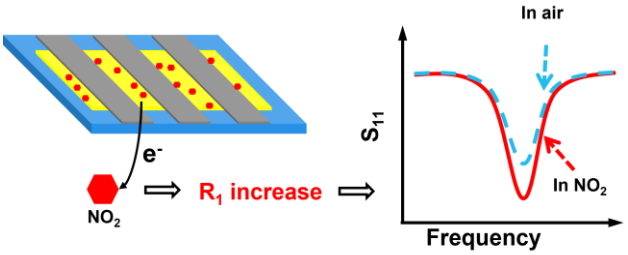

Figure 15. Schematic diagram of sensing mechanism of the LC gas sensor to NO_2.

When the sensor is upon exposure to NO_2, the surface of ZnO NWs becomes chemisorbed with NO_2. This chemisorbed state of NO_2^- further traps electrons in the conduction band of ZnO and reacts with the surface adsorbed oxygen. Both reactions lead to the capture of extra electrons from the ZnO conduction band and expansion of the depletion layer, causing a reduction in carrier concentration. Consequently, this results in an increase in ZnO NWs resistance and ultimately an increase in S_{11}. The corresponding reaction equations are provided as follows.

$$NO_2(g) \rightarrow NO_2(ads) \quad (14)$$

$$NO_2(ads) + O^-(ads) + 2e^- \rightarrow NO_2^-(ads) + O^{2-}(ads) \quad (15)$$

$$NO_2(ads) + e^- \rightarrow NO_2^-(ads) \quad (16)$$

When the sensor is upon exposure to air again, NO_2 molecules are desorbed from the surface of ZnO NWs, and the reaction proceeds in reverse. Electrons seized by NO_2 are released back into the conduction band of the material, causing an increase in carrier concentration and a decrease in the electron depletion layer. These changes eventually result in a reduction in resistance of the sensor and a corresponding decrease in S_{11} magnitude value, which gradually returns to its initial value.

4. Conclusions

A new LC gas sensor with a novel sensor structure was successfully developed, in which the IDC of the LC sensor no longer contacted the substrate, reducing the adverse effect of the substrate. Following measurement, it is found that the VSWR of the designed sensor antenna was 1.238, which is less than 1.5, and the S_{11} parameter of the LC sensor

remained below -10 dB both before and after exposure to NO_2, indicating an effective improvement in transfer efficiency between the reader antenna and the LC antenna. A comprehensive study of the gas sensing property for the prepared LC sensor to NO_2 was fully conducted, and the results revealed that the optimal operating temperature was 180 °C. At this temperature, the sensor showed high response of 1.058 towards NO_2 and a low detection limit of 0.5 ppm NO_2, while maintaining stable during the 60-day testing period. Moreover, this work provides a novel sensor structure based on the inductive coupling principle, broadening the range of substrate options, and significantly reducing interference from the sensor substrate during testing.

Author Contributions: Conceptualization, Z.Y. Liu and Y.B. Shen; methodology, S.K. Zhao; validation, J.Z. Bai and R.X. Ma; investigation, Z.Y. Liu; writing—original draft preparation, S.L. Gao; writing—review and editing, W.G. Liu; supervision, Q. Zhao; project administration, Y.B. Shen. All authors have read and agreed to the published version of the manuscript.

Funding: This research received no external funding.

Acknowledgments: This work was financially supported by the National Natural Science Foundation of China [52274255]; National Key R&D Program of China [2020YFB2008702]; Fundamental Research Funds for the Central Universities [N2201008, N2201004]; Special thanks are due to the instrument and data analysis from Analytica and Test Center, Northeastern University.

Conflicts of Interest: The authors declare no conflict of interest.

References

1. Samerjai, T.; Tamaekong, N.; Liewhiran, C.; Wisitsoraat, A.; Phanichphant, S. NO_2 gas sensing of flame-made Pt-loaded WO_3 thick films. *Journal of Solid State Chemistry* **2014**, *214*, 47-52, doi:10.1016/j.jssc.2013.10.041.
2. Zhao, S.; Shen, Y.; Maboudian, R.; Carraro, C.; Han, C.; Liu, W.; Wei, D. Facile synthesis of ZnO-SnO_2 hetero-structured nanowires for high-performance NO_2 sensing application. *Sensors and Actuators B: Chemical* **2021**, *333*, doi:10.1016/j.snb.2021.129613.
3. Liu, W.; Xu, L.; Sheng, K.; Chen, C.; Zhou, X.; Dong, B.; Bai, X.; Zhang, S.; Lu, G.; Song, H. APTES-functionalized thin-walled porous WO_3 nanotubes for highly selective sensing of NO_2 in a polluted environment. *Journal of Materials Chemistry A* **2018**, *6*, 10976-10989, doi:10.1039/c8ta02452a.
4. Qin, Y.; Wang, F.; Shen, W.; Hu, M. Mesoporous three-dimensional network of crystalline WO_3 nanowires for gas sensing application. *Journal of Alloys and Compounds* **2012**, *540*, 21-26, doi:10.1016/j.jallcom.2012.06.058.
5. Shen, Y.; Bi, H.; Li, T.; Zhong, X.; Chen, X.; Fan, A.; Wei, D. Low-temperature and highly enhanced NO_2 sensing performance of Au-functionalized WO_3 microspheres with a hierarchical nanostructure. *Applied Surface Science* **2018**, *434*, 922-931, doi:10.1016/j.apsusc.2017.11.046.
6. Ghosh, A.; Zhang, C.; Shi, S.; Zhang, H. High temperature CO_2 sensing and its cross-sensitivity towards H_2 and CO gas using calcium doped ZnO thin film coated langasite SAW sensor. *Sensors and Actuators B: Chemical* **2019**, *301*, doi:10.1016/j.snb.2019.126958.
7. Luo, J.; Feng, X.; Kan, H.; Li, H.; Fu, C. One-Dimensional Bi2S3 Nanobelts-Based Surface Acoustic Wave Sensor for NO_2 Detection at Room Temperature. *IEEE Sensors Journal* **2021**, *21*, 1404-1408, doi:10.1109/jsen.2020.3020301.
8. Wen, C.B.; Ju, Y.F.; Li, W.L.; Sun, W.Z.; Xu, X.; Shao, Y.; Li, Y.M.; Wen, L.M. Carbon Dioxide Gas Sensor Using SAW Device Based on ZnO Film. *Applied Mechanics and Materials* **2011**, *135-136*, 347-352, doi:10.4028/www.scientific.net/AMM.135-136.347.
9. Kamada, T.; Ueda, T.; Fukuura, S.; Yumura, T.; Hosokawa, S.; Tanaka, T.; Kan, D.; Shimakawa, Y. Ultralong Distance Hydrogen Spillover Enabled by Valence Changes in a Metal Oxide Surface. *J Am Chem Soc* **2023**, *145*, 1631-1637, doi:10.1021/jacs.2c09729.
10. Zhang, C.; Wang, L.-F.; Huang, J.-Q.; Huang, Q.-A. An LC-Type Passive Wireless Humidity Sensor System With Portable Telemetry Unit. *Journal of Microelectromechanical Systems* **2015**, *24*, 575-581, doi:10.1109/jmems.2014.2333747.
11. Jang, C.; Park, J.K.; Yun, G.H.; Choi, H.H.; Lee, H.J.; Yook, J.G. Radio-Frequency/Microwave Gas Sensors Using Conducting Polymer. *Materials (Basel)* **2020**, *13*, doi:10.3390/ma13122859.
12. Wang, N.; Zhang, N.; Wang, T.; Liu, F.; Wang, X.; Yan, X.; Wang, C.; Liu, X.; Sun, P.; Lu, G. Microwave gas sensor for detection of ammonia at room-temperature. *Sensors and Actuators B: Chemical* **2022**, *350*, doi:10.1016/j.snb.2021.130854.
13. Tan, Q.; Luo, T.; Wei, T.; Liu, J.; Lin, L.; Xiong, J. A Wireless Passive Pressure and Temperature Sensor via a Dual LC Resonant Circuit in Harsh Environments. *Journal of Microelectromechanical Systems* **2017**, *26*, 351-356, doi:10.1109/jmems.2016.2642580.
14. Huang, Q.-A.; Dong, L.; Wang, L.-F. LC Passive Wireless Sensors Toward a Wireless Sensing Platform: Status, Prospects, and Challenges. *Journal of Microelectromechanical Systems* **2016**, *25*, 822-841, doi:10.1109/jmems.2016.2602298.

15. Potyrailo, R.A.; Surman, C.; Nagraj, N.; Burns, A. Materials and Transducers Toward Selective Wireless Gas Sensing. *Chemical Reviews* **2011**, *111*, 7315-7354, doi:10.1021/cr2000477.
16. Azzarelli, J.M.; Mirica, K.A.; Ravnsbaek, J.B.; Swager, T.M. Wireless gas detection with a smartphone via rf communication. *Proceedings of the National Academy of Sciences of the United States of America* **2014**, *111*, 18162-18166, doi:10.1073/pnas.1415403111.
17. Ma, M.; Khan, H.; Shan, W.; Wang, Y.; Ou, J.Z.; Liu, Z.; Kalantar-zadeh, K.; Li, Y. A novel wireless gas sensor based on LTCC technology. *Sensors and Actuators B: Chemical* **2017**, *239*, 711-717, doi:10.1016/j.snb.2016.08.073.
18. Ma, Z.; Chen, P.; Cheng, W.; Yan, K.; Pan, L.; Shi, Y.; Yu, G. Highly Sensitive, Printable Nanostructured Conductive Polymer Wireless Sensor for Food Spoilage Detection. *Nano Lett* **2018**, *18*, 4570-4575, doi:10.1021/acs.nanolett.8b01825.
19. Tang, N.; Zhou, C.; Xu, L.; Jiang, Y.; Qu, H.; Duan, X. A Fully Integrated Wireless Flexible Ammonia Sensor Fabricated by Soft Nano-Lithography. *ACS Sens* **2019**, *4*, 726-732, doi:10.1021/acssensors.8b01690.
20. Zhang, L.; Yang, H.; Tan, Q.; Jing, L.; Zhang, W.; Xiong, J.; Chen, P.-Y. Wireless Detection of Biogenic Amines Using a Split-Ring Resonator with Silver Nanoparticles-Decorated Molybdenum Disulfide. *Sensors and Actuators B: Chemical* **2021**, *343*, doi:10.1016/j.snb.2021.130155.
21. Li, W.; Liang, T.; Liu, W.; Jia, P.; Chen, Y.; Xiong, J.; Lei, C.; Hong, Y.; Li, Y. Wireless passive pressure sensor based on sapphire direct bonding for harsh environments. *Sensors and Actuators a-Physical* **2018**, *280*, 406-412, doi:10.1016/j.sna.2018.08.020.
22. Kim, S.-Y.; Kim, J.; Cheong, W.H.; Lee, I.J.; Lee, H.; Im, H.-G.; Kong, H.; Bae, B.-S.; Park, J.-U. Alcohol gas sensors capable of wireless detection using In_2O_3/Pt nanoparticles and Ag nanowires. *Sensors and Actuators B: Chemical* **2018**, *259*, 825-832, doi:10.1016/j.snb.2017.12.139.
23. Zhang, D.; Yang, Z.; Li, P.; Pang, M.; Xue, Q. Flexible self-powered high-performance ammonia sensor based on Au-decorated $MoSe_2$ nanoflowers driven by single layer MoS_2-flake piezoelectric nanogenerator. *Nano Energy* **2019**, *65*, doi:10.1016/j.nanoen.2019.103974.
24. Zhao, S.; Shen, Y.; Zhou, P.; Hao, F.; Xu, X.; Gao, S.; Wei, D.; Ao, Y.; Shen, Y. Enhanced NO_2 sensing performance of ZnO nanowires functionalized with ultra-fine In_2O_3 nanoparticles. *Sensors and Actuators B: Chemical* **2020**, *308*, doi:10.1016/j.snb.2020.127729.
25. Zhao, S.; Shen, Y.; Yan, X.; Zhou, P.; Yin, Y.; Lu, R.; Han, C.; Cui, B.; Wei, D. Complex-surfactant-assisted hydrothermal synthesis of one-dimensional ZnO nanorods for high-performance ethanol gas sensor. *Sensors and Actuators B: Chemical* **2019**, *286*, 501-511, doi:10.1016/j.snb.2019.01.127.
26. Fiddes, L.K.; Yan, N. RFID tags for wireless electrochemical detection of volatile chemicals. *Sensors and Actuators B: Chemical* **2013**, *186*, 817-823, doi:10.1016/j.snb.2013.05.008.
27. Hasan, N.; Noordin, N.H.; Karim, M.S.A.; Rejab, M.R.M.; Ma, Q.J. Dielectric properties of epoxy–barium titanate composite for 5 GHz microstrip antenna design. *SN Applied Sciences* **2019**, *2*, doi:10.1007/s42452-019-1801-9.
28. Zhang, L.; Tan, Q.; Kou, H.; Wu, D.; Zhang, W.; Xiong, J. Highly Sensitive NH_3 Wireless Sensor Based on Ag-RGO Composite Operated at Room-temperature. *Sci Rep* **2019**, *9*, 9942, doi:10.1038/s41598-019-46213-9.
29. Mao, S.; Cui, S.; Lu, G.; Yu, K.; Wen, Z.; Chen, J. Tuning gas-sensing properties of reduced graphene oxide using tin oxide nanocrystals. *Journal of Materials Chemistry* **2012**, *22*, doi:10.1039/c2jm30378g.
30. Wilson, W.C.; Atkinson, G.M. Passive Wireless Sensor Applications for NASA's Extreme Aeronautical Environments. *IEEE Sensors Journal* **2014**, *14*, 3745-3753, doi:10.1109/jsen.2014.2322959.
31. Klingshirn, C. ZnO: material, physics and applications. *Chemphyschem* **2007**, *8*, 782-803, doi:10.1002/cphc.200700002.
32. Liu, B.; Zeng, H.C.J.J.a.c.s. Hydrothermal synthesis of ZnO nanorods in the diameter regime of 50 nm. **2003**, *125*, 4430.
33. Shimpi, N.G.; Jain, S.; Karmakar, N.; Shah, A.; Kothari, D.C.; Mishra, S. Synthesis of ZnO nanopencils using wet chemical method and its investigation as LPG sensor. *Applied Surface Science* **2016**, *390*, 17-24, doi:10.1016/j.apsusc.2016.08.050.
34. Choi, K.-I.; Hwang, S.-J.; Dai, Z.; Chan Kang, Y.; Lee, J.-H. Rh-catalyzed WO_3 with anomalous humidity dependence of gas sensing characteristics. *RSC Adv.* **2014**, *4*, 53130-53136, doi:10.1039/c4ra06654e.
35. Li, W.; Ma, S.; Li, Y.; Yang, G.; Mao, Y.; Luo, J.; Gengzang, D.; Xu, X.; Yan, S. Enhanced ethanol sensing performance of hollow ZnO–SnO_2 core–shell nanofibers. *Sensors and Actuators B: Chemical* **2015**, *211*, 392-402, doi:10.1016/j.snb.2015.01.090.
36. Li, G.; Shen, Y.; Zhao, S.; Bai, J.; Gao, S.; Liu, W.; Wei, D.; Meng, D.; San, X. Construction of rGO-SnO_2 heterojunction for enhanced hydrogen detection. *Applied Surface Science* **2022**, *585*, doi:10.1016/j.apsusc.2022.152623.
37. Zhao, S.; Shen, Y.; Hao, F.; Kang, C.; Cui, B.; Wei, D.; Meng, F. P-n junctions based on CuO-decorated ZnO nanowires for ethanol sensing application. *Applied Surface Science* **2021**, *538*, doi:10.1016/j.apsusc.2020.148140.
38. Shen, Y.; Wang, W.; Chen, X.; Zhang, B.; Wei, D.; Gao, S.; Cui, B.J.J.o.M.C.A. Nitrogen dioxide sensing using tungsten oxide microspheres with hierarchical nanorod-assembled architectures by a complexing surfactant-mediated hydrothermal route. **2016**, *4*, 1345-1352.
39. Barreca, D.; Bekermann, D.; Comini, E.; Devi, A.; Fischer, R.A.; Gasparotto, A.; Maccato, C.; Sberveglieri, G.; Tondello, E. 1D ZnO nano-assemblies by Plasma-CVD as chemical sensors for flammable and toxic gases. *Sensors and Actuators B: Chemical* **2010**, *149*, 1-7, doi:10.1016/j.snb.2010.06.048.
40. Chang, S.C. Oxygen chemisorption on tin oxide: Correlation between electrical conductivity and EPR measurements. *Journal of Vacuum Science and Technology* **1980**, *17*, 366-369, doi:10.1116/1.570389.

 doi:10.20944/preprints202305.0866.v1

41. Mizokawa, Y.; Nakamura, S.J.O.B. ESR study of adsorbed oxygen on tin dioxide. **1977**, *46*, 580-584.
42. Belysheva, T.V.; Bogovtseva, L.P.; Kazachkov, E.A.; Serebryakova, N.V. Gas-Sensing Properties of Doped In_2O_3 Films as Sensors for NO_2 in Air. *Journal of Analytical Chemistry* **2003**, *58*, 583-587, doi:10.1023/A:1024176505338.
43. Ferro, R.; Rodríguez, J.A.; Bertrand, P. Peculiarities of nitrogen dioxide detection with sprayed undoped and indium-doped zinc oxide thin films. *Thin Solid Films* **2008**, *516*, 2225-2230, doi:10.1016/j.tsf.2007.07.189.